Low–pressure granulite–facies metamorphism in the Southern Chinese Altay orogenic belt, NW China: P–T estimates, U–Pb ages and tectonic implications

Zhao Liu[a,b,c,d,*], Laixi Tong[c], Omar Bartoli[d], Bruna B. Carvalho[d], Chao Li[a,b]

[a] State Key Laboratory of Isotope Geochemistry, Guangzhou Institute of Geochemistry, Chinese Academy of Sciences, Guangzhou 510640, China
[b] University of Chinese Academy of Sciences, Beijing 100049, China
[c] State Key Laboratory of Continental Dynamics, Department of Geology, Northwest University, Xi'an 710069, China
[d] Dipartimento di Geoscienze, Università di Padova, Via Gradenigo 6, 35131 Padua, Italy

ARTICLE INFO

ABSTRACT

The Chinese Altay orogenic belt formed in the Paleozoic is an important part of the Central Asian Orogenic Belt (CAOB), accompanying with remarkable metamorphism. Its tectono–metamorphic evolution history is still a controversial topic. In this contribution, we investigate the petrography, metamorphic peak P–T conditions and zircon geochronology of the newly discovered garnet–absent metapelitic and felsic gneisses at Wuqiagou area in the southern Chinese Altay. They are characterized by an assemblage of orthopyroxene + biotite + plagioclase + quartz + Fe–Ti oxides ± cordierite ± K–feldspar, in which most K–feldspar grains have transformed into perthites with thin albite lamellae. The Wuqiagou garnet–absent gneisses experienced pervasive partial melting, as testified by microstructures such as mineral pseudomorphs after melt films or pockets. Phase diagram modelling constrains the peak P–T conditions to 3.5–5.5 kbar and 800–900 °C, with possible geothermal gradients of 45–75 °C/km, indicative of a prominent low–pressure granulite–facies metamorphic event in the southern Chinese Altay. SIMS zircon U–Pb dating results show a weighted mean age of 255.8 ± 1.8 Ma. This age is interpreted to represent the timing of this low–pressure granulite facies metamorphism, which is highly coeval with the timing of their hosted mafic granulite lenses (~255 Ma) and nearby mantle–derived mafic intrusions (~257 Ma). Based on available petrological, geochemical and chronological data, we propose that the Permian low–pressure granulite–facies metamorphic event in the southern Chinese Altay was likely associated with the intrusions of deep–derived mafic magma at a relatively shallow crustal level (12–18 km) in a post–orogenic extensional setting, with a possible link with the Tarim mantle plume activity.

1. Introduction

Low–pressure–high–temperature (LP–HT) metamorphism has occurred throughout the world, which was usually defined for a P–T range of > 600 °C and < 4 kbar (Thompson and England, 1984; De Yoreo et al., 1991; Langone et al., 2010). However, the peak pressure could reach higher values with increasing temperature, especially when rocks experience the granulite–facies metamorphism (4–6 kbar; Schreurs and Westra, 1986; Bindu, 1997; Buick et al., 1998; Li and Zhang, 2004; Tropper et al., 2006; Sreejith and Kumar, 2012; Morrissey et al., 2014), namely low–pressure granulite–facies metamorphism.

LP–HT metamorphic belts usually occurred in specific tectonic settings with steep geothermal gradients (60–150 °C km⁻¹) (e.g., Thompson and England, 1984; Barton and Hanson, 1989; Sandiford et al., 1998; Langone et al., 2010; Okay et al., 2014). So far, it was found in distinct tectonic settings, including magmatic arc (Li and Zhang, 2004; JANOUŠEK et al., 2006), extensional tectonic setting (Wickham and Oxburgh, 1985; Lucassen and Franz, 1996; Langone et al., 2010; Okay et al., 2014; Zhang et al., 2018), and continent–continent collision zone (Lux et al., 1986) (Supplementary File S1). In most cases, LP–HT metamorphism was associated with syn– to post–orogenic mafic and granitic plutonic activities (Barton and Hanson, 1989; De Yoreo et al., 1991; Craven et al., 2012). Determination of the genetic mechanism of the metamorphism largely relies on precise constraints on the metamorphic conditions, which subsequently, have to be related to the known potential heat sources in terms of space and time (Craven et al., 2012).

The Chinese Altay orogenic belt is an important part of the Central

Asian Orogenic Belt (CAOB), and is considered as a key to understand its accretionary orogenic processes (e.g., Jahn et al., 2004; Xiao et al., 2004; He et al., 2018; Windley and Xiao, 2018). In the last 15 years, some metapelitic and mafic granulites with ages of 293–260 Ma have been reported from the Chinese Altay orogenic belt (Supplementary File S2; Li et al., 2004, 2014; Chen et al., 2006; Wang et al., 2009b; Tong et al., 2014; Yang et al., 2015b; Liu et al., 2020), some of which have even reached ultrahigh–temperature (UHT) metamorphic conditions (Li et al., 2014; Tong et al., 2014; Yang et al., 2015b; Liu et al., 2020). Up to now, researchers have proposed various genetic models to explain the Altay HT–UHT metamorphism, such as Paleo–Asian oceanic crustal subduction (Li et al., 2004; Chen et al., 2006), collision of the Junggar arc with the Chinese Altay terrane (Broussolle et al., 2018), slab break–off (Li et al., 2014; Yang et al., 2015b), ridge–subduction (Windley and Xiao, 2018), and the thermal pulse of Tarim mantle plume activities (e.g., Tong et al., 2014; Yang et al., 2015a; Liu et al., 2019, 2020). However, until recently, the tectonic nature of the southern Chinese Altay is still a controversial and debated topic.

In this contribution, we investigate the petrography, mineral chemistry, P–T estimates and geochronology of the newly recognized garnet–absent metapelitic and felsic gneisses at Wuqiagou area, in Fuyun county. Petrographical observations and phase equilibrium modelling suggest that they have reached granulite–facies metamorphic conditions and experienced partial melting with microstructural evidence of melt films and pockets pseudomorphed by plagioclase and quartz. This study will increase our understanding of the Permian metamorphism in the southern Chinese Altay, because the investigated samples provide evidence of metamorphism of the relatively shallow crustal rocks. The spatial and temporal relationships between LP–HT metamorphism and mafic plutonic activities are also elucidated. Accordingly, the LP–HT metamorphic rocks cropping out in this region are a key element in evaluating the thermal conditions and understanding the tectonic history of the Chinese Altay.

2. Geological background

The NW–SE trending Chinese Altay orogenic belt is bounded by the Siberian plate to the north and the Kazakhstan–Junggar plate to the south (Fig. 1) (Windley et al., 2007), which comprises various lithological types, mainly including volcanic rocks, high grade metamorphic rocks and large volumes of granitoids (Windley et al., 2002; Jiang et al., 2015). Five fault–bounded terranes have been previously proposed based on the stratigraphy, metamorphism, deformation patterns and chronology (Windley et al., 2002; Xiao et al., 2004; Wang et al., 2006, 2009a). However, these terranes show close affinities, which are probably resulted from juxtaposition of different crustal levels, as pointed out by Jiang et al. (2015, 2019) and Broussolle et al. (2018, 2019).

The tectonic evolution of the Chinese Altay orogen mainly involves five scenarios based on previous studies (Windley et al., 2002, 2007; Wang et al., 2006; Long et al., 2007; Sun et al., 2009; Yang et al., 2011; Zhang et al., 2012; Wang et al., 2009b, 2014; Li et al., 2014; Tong et al., 2014; Liu et al., 2020): (i) a passive continental margin or peri––Gondwana terrane during the Neoproterozoic–early Paleozoic; (ii) the development of a late Silurian to early Devonian arc environment related to the northward subduction of Junggar plate; (iii) continent–arc collision, subduction of ridge, or the development of a possible back–arc basin in the middle to late Devonian; (iv) Permian (300–260 Ma) post–orogenic setting with a possible overprinting by the Tarim mantle plume; and (v) intraplate magmatism beginning in the Jurassic.

The Chinese Altay was considered to have experienced two dominating tectono–thermal cycles (Zhuang, 1994; Wei et al., 2007; Broussolle et al., 2018; Liu et al., 2020). The first tectono–metamorphic cycle was dated at 390–365 Ma (e.g., Zhuang, 1994; Zheng et al., 2007; Jiang et al., 2010), and considered to be linked with two distinct metamorphic stages characterized by M1 Barrovian–type MT–MP and M2

Buchan–type HT–LP field gradients, with metamorphic degrees ranging from greenschist to amphibolite facies conditions (Jiang et al., 2010, 2015). The Devonian orogenic architecture was subsequently reworked by the Permian HT–UHT metamorphism on its southern margin (e.g., Li et al., 2004, 2014; Wang et al., 2009b; Tong et al., 2014; Jiang et al., 2015; Liu et al., 2020), which was interpreted by Broussolle et al. (2018) as the second tectono–metamorphic cycle in the Chinese Altay. The process was also companied by extensive magmatic activities (Table 1).

Both the UHT granulites and low–pressure garnet–absent gneisses occur along the NW–SE large Erqis fault belt, and sinistral strike–slip motion along the Erqis belt resulted in ductile shearing along this belt in the Permian (290–280 Ma; Laurent–Charvet et al., 2003; Briggs et al., 2007; Zhang et al., 2012). The garnet–absent gneisses occur as large lenses within biotite–plagioclase gneisses. The biotite–plagioclase gneisses and garnet–biotite–plagioclase gneisses usually show gradational contact relationships. Occasionally, the garnet–biotite–plagioclase gneisses contain small Permian UHT granulite lenses (Liu et al., 2020).

3. Sampling and petrography

Orthopyroxene–cordierite–K–feldspar–bearing metapelitic gneiss (sample FY15–04; 46°57′52″ N, 89°38′50″ E) occurs as lenses hosted within biotite–plagioclase gneisses, with two leucocratic veins which are 5–10 cm in width. The size of the lenses is up to $2.5 \times 0.5 \ m^2$. Their gneissosities strike N ~170° with dips of ~75°. Orthopyroxene–cordierite–bearing metapelitic gneiss (sample FY15–14; 46°57′51″ N, 89°39′00″ E) is located near to the mountaintop, which is close to the mafic granulites described by Liu et al. (2019). Orthopyroxene–K–feldspar–bearing felsic gneiss (sample FY15–32; 46°57′59″ N, 89°38′46″ E) occurred as country rocks of fine–grained two–pyroxene mafic granulite (Fig. 2), and its gneissosity striked N ~340° with steep dips of 80–85°.

Metapelitic gneiss FY15–04 is fine–grained and displays a weak gneissic structure. It is characterized by an assemblage of orthopyroxene (7–8%), cordierite (10–15%), biotite (15–20%), plagioclase (15–20%), K–feldspar (25–30%) and quartz (10–15%), with accessory ilmenite, monazite and zircon (< 5%) (Fig. 3a–c). This sample contains a weak WS–dipping foliation (240°∠33°) mainly defined by biotite and felsic minerals. Few orthopyroxene grains are relatively large in size (0.2–0.3 mm) and are widely replaced by retrograde biotite (Fig. 3a). K–feldspar is an albite–K–feldspar solid solution with albite (ab) contents ranging from 5 to 19 mol.% (Fig. 3c). Few plagioclase crystals are included in biotite and perthite (Fig. 3c). Biotite may also occur as small inclusions within the perthites (Fig. 3b), and their disposition could indicate a pre–peak foliation. Most biotite flakes and some quartz grains are irregular and fill the intergranular pores, indicative of a retrograde origin (see below).

Metapelitic gneiss FY15–14 is dark gray in colour, and dominantly composed of orthopyroxene (8–12%), cordierite (20–25%), biotite (15–25%), plagioclase (20–30%) and quartz (10–18%) (Fig. 3d and e). Accessory minerals such as magnetite, ilmenite and zircon are rare. On the thin section scale, orthopyroxene, cordierite, biotite and when preserved, plagioclase, are aligned and define the main foliation. Orthopyroxene (0.02 to 0.4 mm in diameter) is euhedral to anhedral, and generally contains inclusions of quartz, biotite and ilmenite (Fig. 3e). Small orthopyroxene grains occur throughout the sample (Fig. 3d). Biotite usually occurs as small flakes or tabular poikiloblasts, and is hosted in the matrix dominated by orthopyroxene, plagioclase, cordierite and quartz (Fig. 3d). Tiny biotite inclusions in other minerals are ascribed to the pre–peak minerals. Biotite poikiloblasts define the major foliation and in some cases, have inclusions of orthopyroxene, cordierite, plagioclase, quartz and opaque minerals (Fig. 3d and e). Plagioclase and cordierite in the matrix are generally less than 0.2 mm in length (Fig. 3e). Some plagioclase contains quartz and tiny biotite
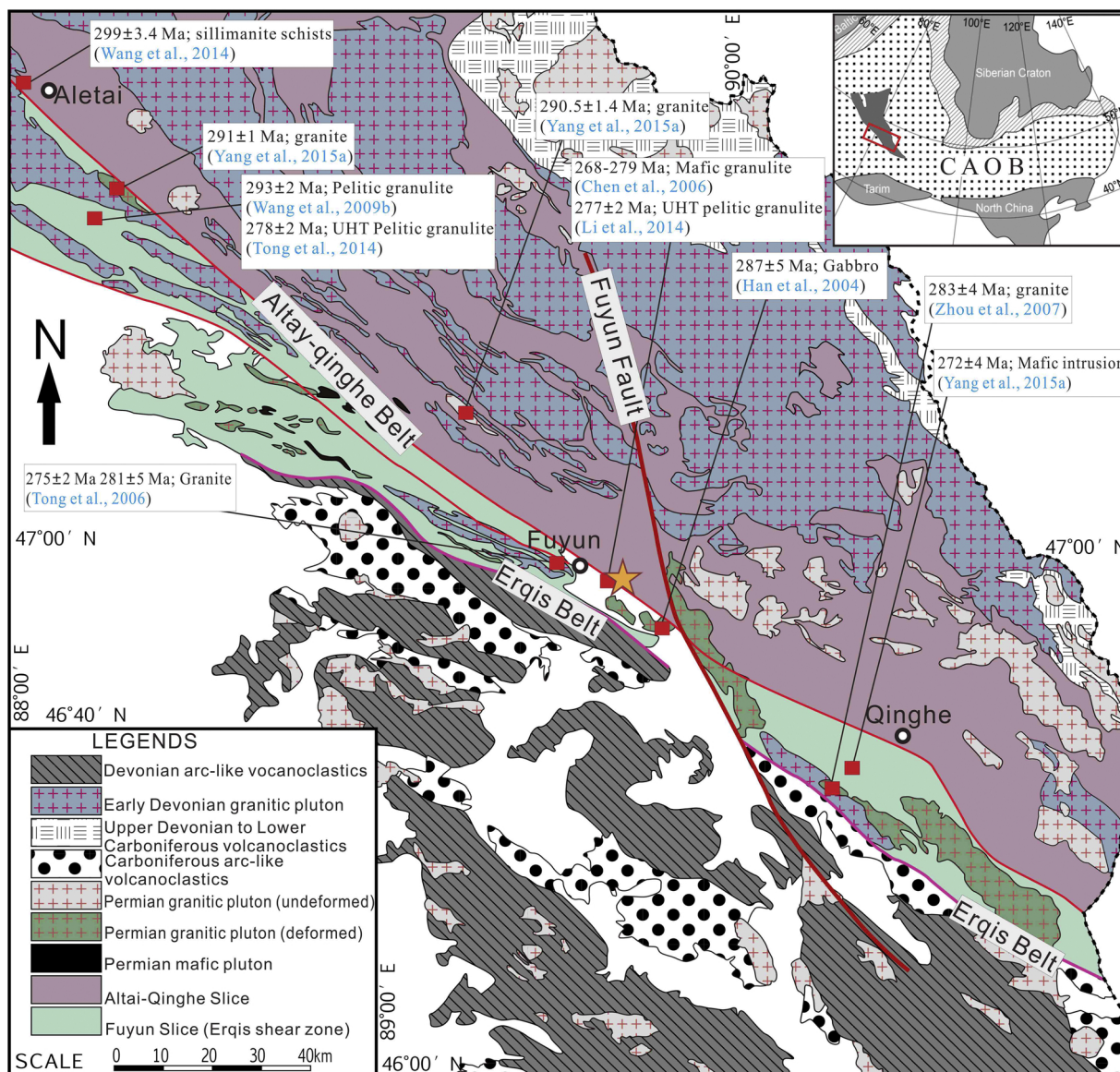
Fig. 1. Geological map of part of Northern Xinjiang, NW China (modified after 4 geological maps with scale 1/200,000, The Team One of Geological Survey of Xinjiang, 1979; Yang et al., 2015a) showing the main tectonic units and previous chronological data from the literature.

inclusions. Cordierite with orthopyroxene and quartz inclusions is also common. No K–feldspar is observed in this sample.

Felsic gneiss sample FY15–32 displays banded structure and comprises orthopyroxene (10–15%), biotite (8–15%), plagioclase (5–10%), K–feldspar (50–55%), quartz (10–15%) and Fe–Ti oxides (5–10%) (Fig. 3f, g and h). The gneiss sample is composed of dark bandings (15–30%) and felsic matrix (70–85%). Orthopyroxene, biotite and Fe–Ti oxide minerals form the dark bandings, while the felsic portion is mainly composed of K–feldspar and rare quartz (Fig. 3g). Most K–feldspars have transformed into perthites with thin albite lamellae of less than 5 μm (Fig. 3g). Albite contents range from 5 to 24 mol.%. Plagioclase is commonly crystallized around K–feldspar and occurs as irregular interstitial grains or micro–veins. Radial biotite is also observed to grow on opaque minerals mainly composed of ilmenite and magnetite (Fig. 3g). In this case, magnetite was also found to grow on ilmenite (Fig. 3h). Tiny pre–peak biotite is partly or totally enclosed within quartz or K–feldspar.

The investigated samples are partially melted rocks. The cuspate–lobate boundaries of quartz against other minerals in the matrix of sample FY15–14 (Fig. 4a and b), and the plagioclase and quartz grains

within the pores bounded by K–feldspar in rock FY15–32 (Fig. 4c and d) are clear microstructures indicating the presence of a former melt (Holness et al., 2011; Bartoli et al., 2016). In particular, the interconnected plagioclase and quartz films, lower dihedral angles at the corners of elongated cuspate–shaped plagioclase and quartz grains, and straight boundaries between them represent melt–filled pores and films now pseudomorphosed by minerals (Sawyer, 2008; Holness et al., 2011).

4. Analytical methods

4.1. Whole–rock geochemistry and mineral chemistry

Major element oxides (wt.%) were determined on fused glass disks with a 1:8 sample to $Li_2B_4O_7$ flux ratio, using a Rigaku ZSX100e X–ray fluorescence spectrometer in the Key Laboratory of Isotope Geochronology and Geochemistry, Guangzhou Institute of Geochemistry. The accuracy of the analyses is within 1% for most major elements. Sample preparation techniques and other details of procedures are described in the reference (Long et al., 2011). The

Table 1
Summary of the Permian ages reported from the southern Chinese Altay.

| Locations	Rocks	Methods	Ages (Ma)	References
Fuyun	Gabrro	SHRIMP	274 ± 4	Yang et al. (2015a)
Fuyun	Mafic intrusion	SHRIMP	257, 280	Chen and Han. (2006)
Kalatongke	Mafic complex	SHRIMP	287 ± 5	Han et al. (2004)
Qinghe	Monzogranite	LA-ICP-MS	294 ± 4.6	He et al. (2018)
Lamazhao	Granite	SHRIMP	276 ± 9	Wang et al. (2005)
Qinghe	Granite	SHRIMP	283 ± 4	Zhou et al. (2007)
Fuyun-Qinghe	Granite	SHRIMP	283 ± 4	Zhang et al. (2012)
Fuyun	Granite	LA-ICP-MS	291 ± 9, 294 ± 6	Zhang et al. (2015)
Aletai	Leucogranite	SHRIMP	290, 291	Yang et al. (2015a)
Jieerkuduke	Acidic dyke swarm	LA-ICP-MS	279 ± 3	Shen et al. (2013)
Qinghe	Gneiss	SHRIMP	281 ± 3	Hu et al. (2006)
Aletai	Gneiss	LA-ICP-MS	284 ± 5.5	Yang et al. (2015a)
Fuyun	Gneiss	In situ Th-Pb	278 ± 9, 275 ± 8	Briggs et al. (2007)
Altai-Qinghe	Gneiss	CHIME	261-268	Zheng et al. (2007)
Fuyun	Mafic granulite	SHRIMP	268-279	Chen et al. (2006)
Fuyun	Mafic granulite	SHRIMP	271 ± 3.2	Liu et al. (2019)
Kalasu	Pelitic granulite	SHRIMP	293 ± 2	Wang et al. (2009b)
Kalasu	Pelitic granulite	SHRIMP	278 ± 2	Tong et al. (2014)
Fuyun	Pelitic granulite	LA-ICP-MS	281-288	Liu et al. (2020)
Fuyun	Pelitic granulite	SHRIMP	277 ± 2	Li et al. (2014)
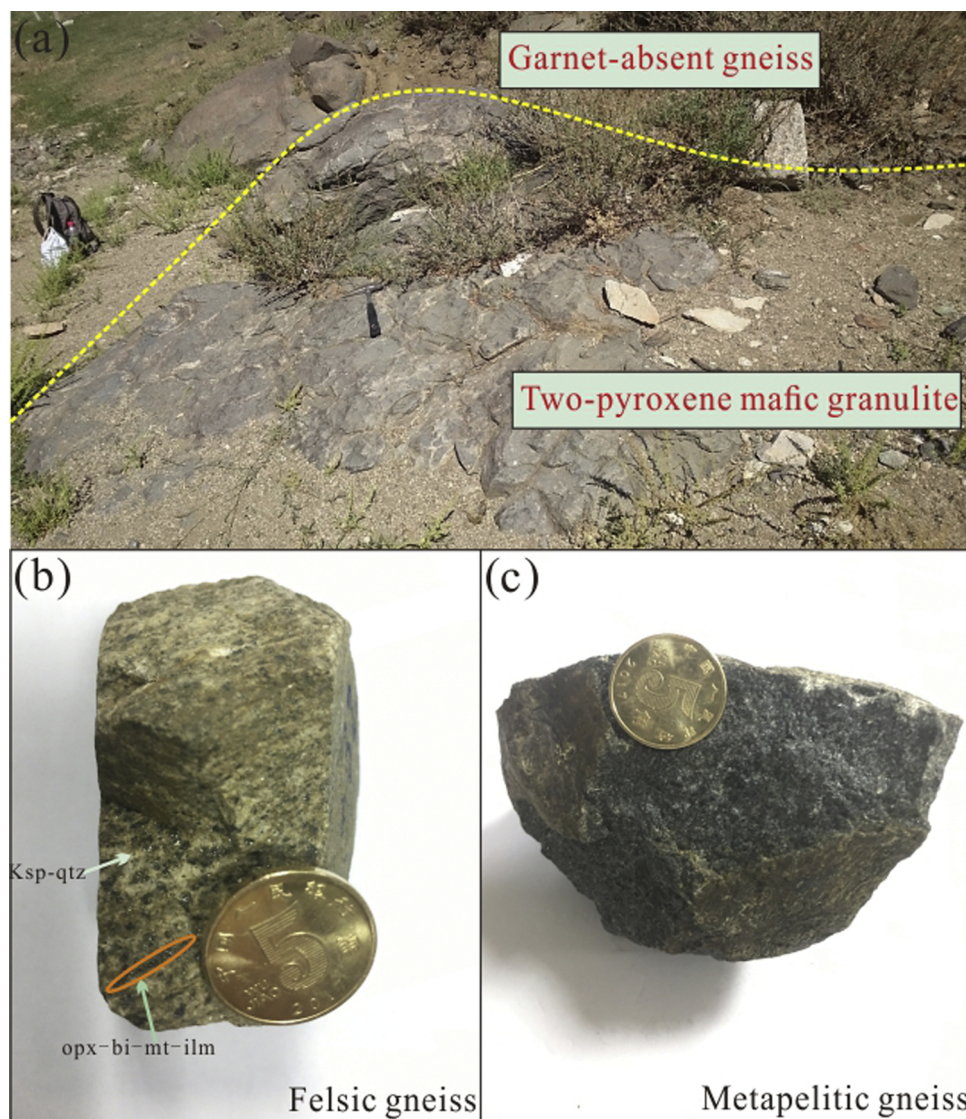
Fig. 2. Photographs showing the field occurrences and hand samples of the Altay garnet–absent gneisses, in which, (b) and (c) are photographs of hand samples of felsic and metapelitic gneisses, respectively. The hammer for scale is about 30 cm long. The coin for scale is 2.05 cm in diameter.
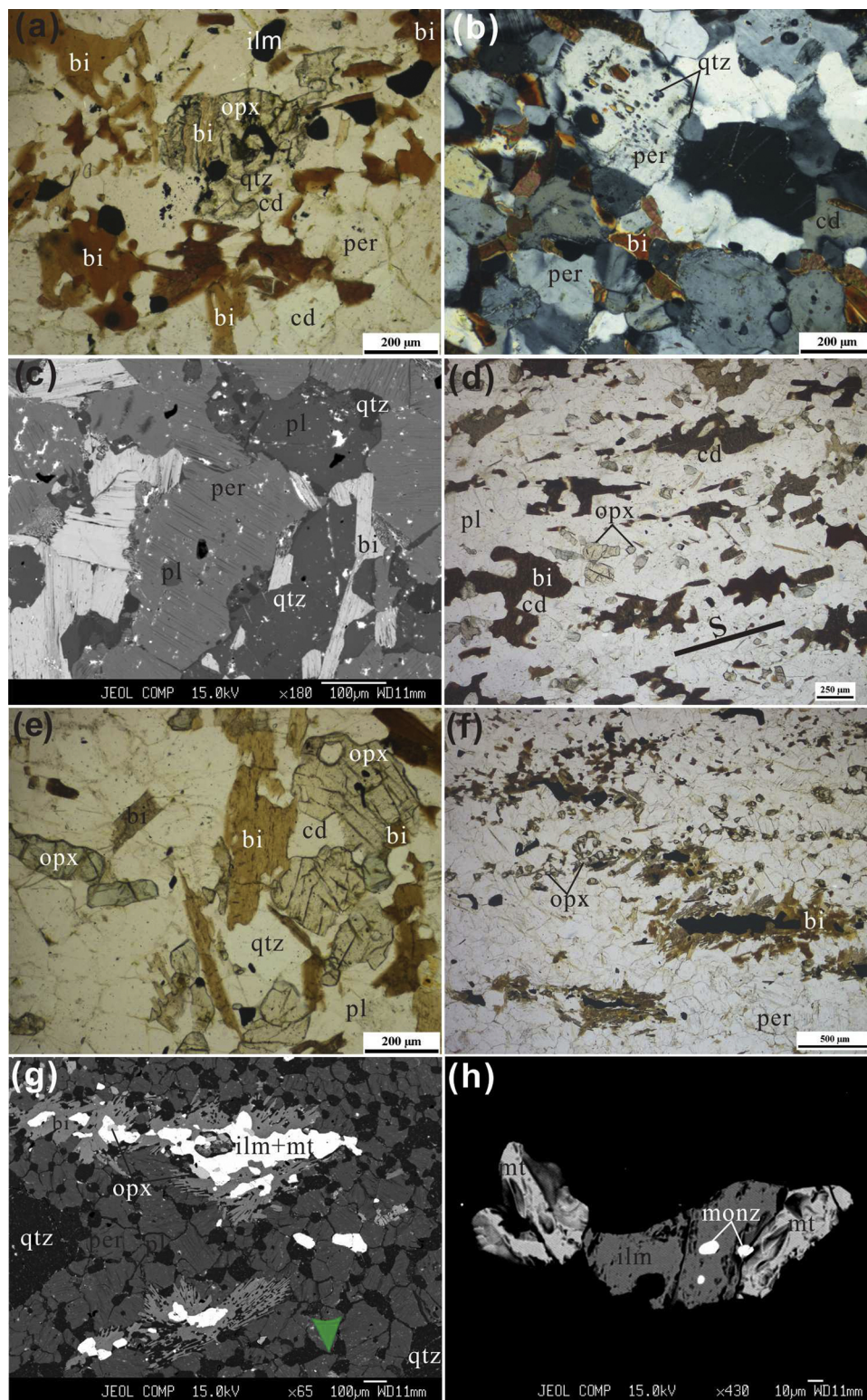
Fig. 3. Photomicrographs and back–scattered electron (BSE) images showing the mineral assemblages and textures in the garnet–absent metapelitic and felsic gneisses from Wuqiagou area, in which, (c), (g) and (h) are BSE images. **a** A large orthopyroxene grain replaced by late biotite (FY15–04). **b** K–feldspar containing oriented inclusions of biotite and quartz (FY15–04). **c** K–feldspar with albite (ab) lamellae and pre–peak plagioclase inclusions (FY15–04). **d** Foliation defined mainly by biotite poikiloblasts (FY15–14). **e** An assemblage of orthopyroxene + cordierite + biotite + plagioclase + quartz in the felsic gneiss sample FY15–14. **f** Banded structure of FY15–32 mainly marked by orthopyroxene, biotite and Fe–Ti oxide phases. **g** Dark banding mainly formed by biotite and Fe–Ti oxide minerals (FY15–32). Plenty of quartz pools occur around K–feldspar in the matrix, suggesting the presence of a large volume of former melt. **h** Magnetite growing on the ilmenite (FY15–32). Mineral abbreviations: opx, orthopyroxene; cd, cordierite; bi, biotite; per, perthite; pl, plagioclase; ksp, K–feldspar; mt, magnetite; ilm, ilmenite; qtz, quartz; monz, monazite.

geochemical data are presented in Supplementary File S3.

Minerals in the Altay garnet–absent gneisses were analyzed with a JXA–8100 microprobe at State Key Laboratory of Isotopic Geochemistry, Guangzhou Institute of Geochemistry, Chinese Academy of Sciences, with an accelerating voltage of 15 kV, a beam current of 3×10^{-8} nÅ, a beam width of 1 μm, and data correction by using a ZAF method. Representative mineral compositions for the studied samples are listed in Supplementary Files S4–S5.

4.2. Zircon geochronology

Conventional magnetic and heavy liquid techniques followed by hand–picking under a binocular microscope were used for zircon separation from Altay metapelitic gneiss sample FY15–04. Zircon cathodoluminescence (CL) images were taken before U–Pb dating analysis using a JEOL JXA–8100. Measurements of U, Th, and Pb were conducted using the Cameca IMS–1280–HR at the State Key Laboratory of
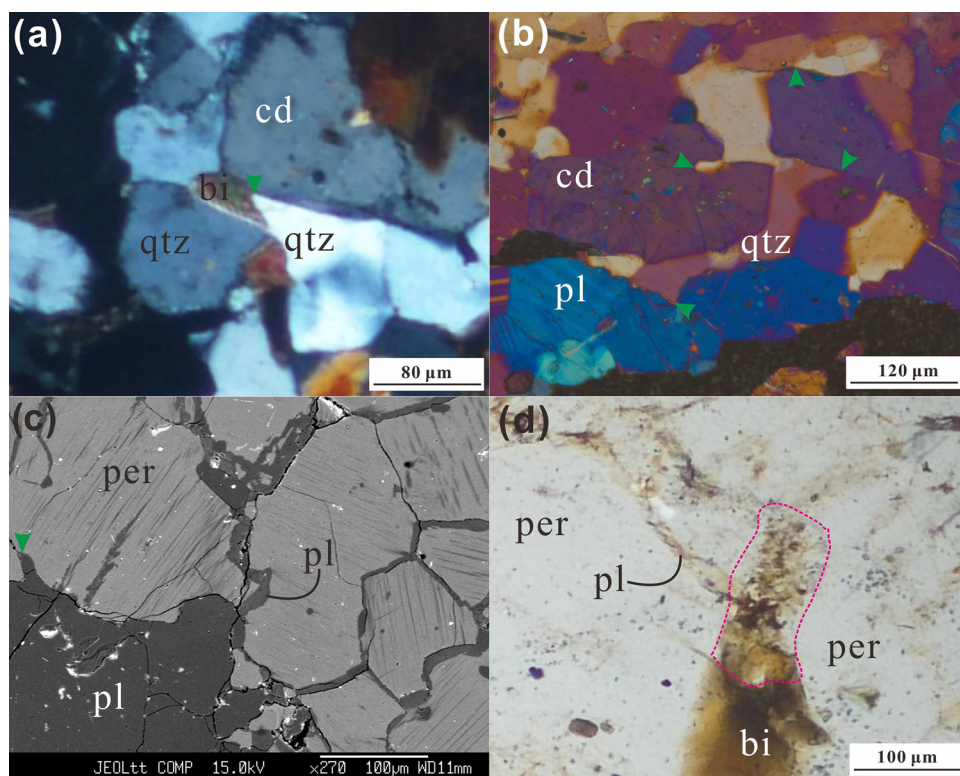
Fig. 4. Photomicrographs and BSE images with evidence of former presence of melt in the investigated rocks. Cuspate–shaped boundaries are considered to be inherited from the former melt, highlighted by green arrows. The relatively straight boundaries of the minerals indicate that they probably crystallized from melt.
a Intergranular biotite and quartz with cuspate boundaries against the surrounding cordierite grains (FY15–04). **b** Highly cuspate quartz grains pseudomorphing the former melt (FY15–14). **c** Sieve–like melt films pseudomorphed by plagioclase, which form a completely interconnected network (FY15–32). The larger plagioclase grain shows elongate cuspate–shape against the surrounding perthites. **d** Melt–filled pores partially filled by plumose intergrowths of biotite and plagioclase. Perthites are usually isolated by pale yellow plagioclase films (FY15–32).
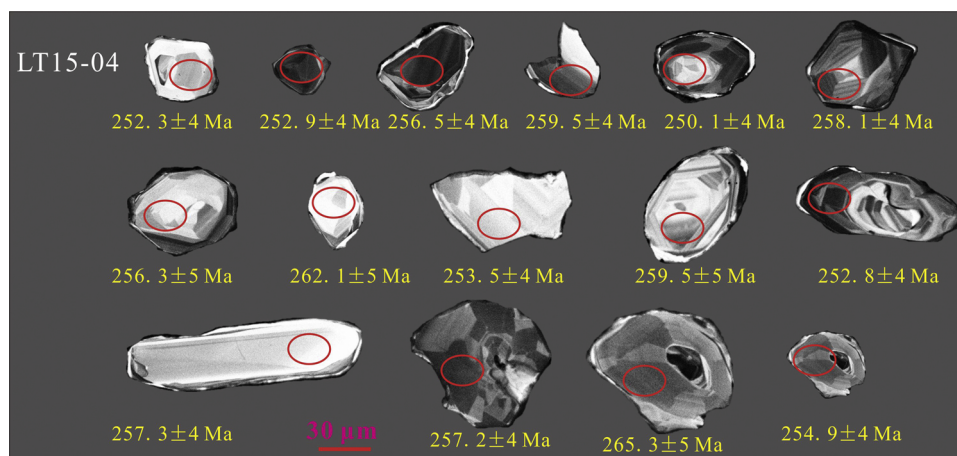

Fig. 5. The CL images for representative zircons in the metapelitic gneiss sample FY15–04.

Isotope Geochemistry, Guangzhou Institute of Geochemistry, Chinese Academy of Sciences. The analytical procedures were similar to those described by Li et al. (2009). The ellipsoidal spot is about 20 × 30 μm in size. U–Th–Pb ratios were determined relative to the standard zircon from ~337 Ma ago Plešovice (Sláma et al., 2008). In order to monitor the external uncertainties of SIMS U–Pb zircon dating calibrated against the Plešovice standard, a second zircon standard Qinghu was alternately analyzed as an unknown together with the other unknown zircons. Seven measurements of the Qinghu zircon yielded a concordia age of 159.2 ± 1.3 Ma, which is identical within error with the recommended value of 159.5 ± 0.2 Ma (Li et al., 2013).

5. Whole–rock geochemistry and mineral chemistry

5.1. Whole–rock geochemistry

The samples have low loss–on–ignition (LOI) that varies from 0.04 to 1.16%. These samples exhibit wide compositional ranges, i.e., SiO_2 = 53.27–69.97 wt.%, Al_2O_3 = 12.00–20.19 wt.%, $Fe_2O_3^T$ = 6.18–13.01 wt.%, and MgO = 3.64–7.23 wt.%, which corresponds to $Mg^{\#}$ values of 21–39. Felsic gneiss sample FY15–32 has markedly higher K_2O contents (~7.7 wt.%) than others, consistent with molar fraction differences of major minerals. Their K_2O + Na_2O contents range from 3.06 to 9.42%, with K_2O/Na_2O ratios ranging from 1.68 to 4.71.

5.2. Mineral chemistry

Orthopyroxene grains in metapelitic gneiss FY15–04 have relatively low $Al_{p.f.u.}$ (= Al/2) contents (0.05–0.07), CaO contents (< 0.11 wt.%) and X_{Mg}(Mg/(Mg + Fe^{2+}) values (0.40–0.43). Cordierite present in the matrix has X_{Mg} values of 0.57–0.59. Cordierite preserved as inclusions in biotite has X_{Mg} values of ~0.59. Biotite in sample FY15–04 has X_{Mg} values of 0.41–0.44 and $Ti_{p.f.u.}$ contents of 0.09–0.12. Plagioclase in the

Table 2
SIMS U–Th–Pb analysis results for zircons from the sample FY15–04.

| Spot	U	Th	Th/U	$^{206}Pb/^{238}U$	1σ	$^{207}Pb*/^{206}Pb*$	1σ	$^{207}Pb*/U^{235}$	1σ	$^{206}Pb/^{238}U(Ma)$	1σ	$^{207}Pb/^{206}Pb(Ma)$	1σ	$^{207}Pb/^{235}U(Ma)$	1σ
1	333	154	0.46	0.040	1.76251	0.050	2.33180	0.273	1.52671	252.3	4	174.9	35	245.0	5
2	145	51	0.36	0.040	1.68525	0.052	2.19452	0.285	1.40565	253.2	4	264.0	32	254.3	5
3	490	252	0.52	0.041	1.58363	0.050	2.01389	0.284	1.24415	258.1	4	214.1	29	253.8	5
4	164	59	0.36	0.040	1.71517	0.052	2.57806	0.286	1.92473	253.8	4	270.9	44	255.5	6
5	245	83	0.34	0.040	1.71035	0.049	2.83267	0.269	2.25803	251.4	4	149.0	52	241.7	6
6	1177	363	0.31	0.040	1.59626	0.046	6.44108	0.254	6.24015	252.9	4	3.6	144	229.5	13
7	194	68	0.35	0.040	1.74414	0.051	2.21148	0.285	1.35965	254.7	4	257.8	31	255.0	5
8	1444	701	0.49	0.041	1.60106	0.051	2.03808	0.288	1.26110	256.5	4	262.2	29	257.1	5
9	665	188	0.28	0.041	1.63274	0.051	3.04402	0.287	2.56909	259.5	4	222.6	58	255.9	7
10	444	146	0.33	0.040	1.64595	0.051	2.76514	0.281	2.22190	250.1	4	262.7	50	251.3	6
11	270	80	0.30	0.047	1.67929	0.174	2.67625	1.119	2.08383	294.4	5	2593.0	34	762.4	14
12	452	147	0.33	0.041	1.70776	0.049	2.20523	0.279	1.39521	258.1	4	169.6	32	249.6	5
13	210	64	0.31	0.041	1.87005	0.054	2.29697	0.301	1.33379	256.3	5	363.6	30	267.2	5
14	161	65	0.40	0.041	2.07904	0.055	2.37562	0.314	1.14943	260.3	5	426.8	25	277.6	6
15	269	80	0.30	0.041	1.92560	0.138	5.94157	0.789	5.62088	262.1	5	2201.2	94	590.6	27
16	273	97	0.35	0.040	1.60362	0.034	########	0.186	########	253.5	4	821.4	298	173.2	18
17	181	61	0.34	0.055	2.08815	0.251	4.11912	1.901	3.55060	345.2	7	3188.7	55	1081.3	28
18	257	93	0.36	0.041	1.77082	0.042	########	0.240	########	259.5	5	202.6	407	218.6	37
19	596	190	0.32	0.040	1.57277	0.051	2.45655	0.280	1.88707	252.8	4	233.3	43	250.9	5
20	190	65	0.34	0.081	2.67854	0.436	3.03336	4.882	1.42362	503.7	13	4037.0	21	1799.1	26
21	385	122	0.32	0.041	1.59968	0.052	2.45247	0.291	1.85893	257.3	4	275.8	42	259.2	6
22	484	144	0.30	0.045	2.09416	0.130	5.72858	0.804	5.33209	283.6	6	2092.5	91	598.9	26
23	1204	195	0.16	0.041	1.73680	0.089	3.87989	0.499	3.46945	257.2	4	1401.4	65	410.9	13
24	782	305	0.39	0.042	1.95366	0.064	2.80096	0.372	2.00714	265.3	5	749.8	42	321.3	8
25	494	150	0.30	0.040	1.58247	0.027	########	0.150	########	254.9	4	1491.5	449	142.2	21
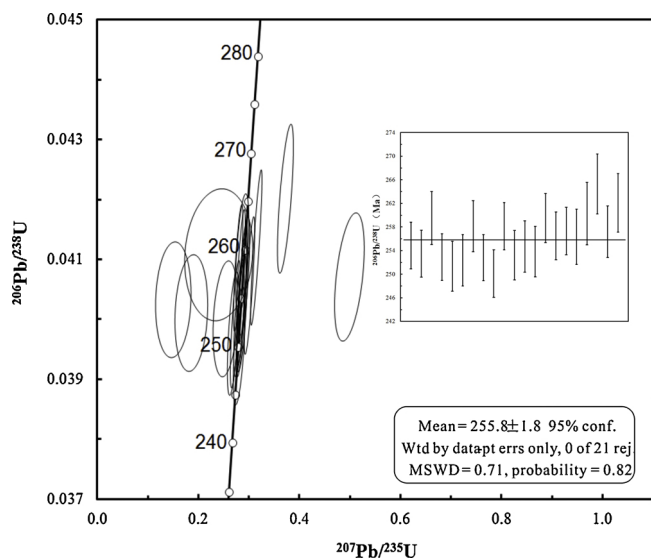
Fig. 6. U–Pb concordant age diagram for zircons in the metapelitic gneiss sample FY15–04.

matrix is andesine, with restricted compositional range (An$_{36–34}$). Plagioclase inclusions preserved in biotite and K–feldspar have albite contents of X$_{An}$ = 0.34. Albite lamellae in perthites have X$_{Ab}$ contents of 0.90–0.97. Homogenous K–feldspar has slightly higher X$_{Or}$ contents than K–feldspar in perthites.

In metapelitic gneiss (FY15–14), orthopyroxenes have X$_{Mg}$ values of 0.45–0.50 and contain low Al$_2$O$_3$ contents (2.51–3.12 wt.%), with corresponding X$_{Al}$ values of 0.05–0.08 p.f.u. The orthopyroxene crystals in the matrix and those preserved as inclusions in biotite have similar compositions. Cordierite in the matrix is rich in MgO, with X$_{Mg}$ values of 0.66–0.69. Cordierite within biotite has a typical X$_{Mg}$ value of ∼0.65. The TiO$_2$ contents of biotite range from 1.82 to 1.97 wt.% (0.10–0.12 p.f.u.) and X$_{Mg}$ values vary from 0.45 to 0.48. Plagioclase crystals from different textural positions have similar composition, which is andesine, showing small compositional ranges (An$_{31–33}$).

Orthopyroxene in felsic gneiss (FY15–32) has low Al$_2$O$_3$ contents of 1.23–1.34 wt.%, with corresponding X$_{Al}$ values of 0.02–0.03 in the formula. There is no clear compositional difference for opx from different textural positions, and they typically have X$_{Mg}$ values of 0.58–0.60. Biotite has relatively high X$_{Mg}$ values (0.59–0.61) and wide Ti$_{p.f.u.}$ compositional variations ranging from 0.10 to 0.27 p.f.u. Biotite inclusions contained in the perthite have a lower X$_{Mg}$ value of ∼0.41, among which, biotite associated with ilmenite contains relatively higher Ti contents. Plagioclase films around K–feldspar have a wider compositional variations ranging from Or$_1$Ab$_{72}$An$_{27}$ to Or$_7$Ab$_{79}$An$_{15}$. Albite lamellae in perthites have a typical X$_{Ab}$ content of ∼0.94. K–feldspar has X$_{Or}$ of 0.86–0.94 and X$_{Ab}$ of 0.06–0.14. Albite lamellae in perthites have X$_{Ab}$ contents of 0.83–0.94.

6. Zircon morphology and U–Pb geochronology

Representative CL images of zircons from the Altay gneiss sample FY15–04 are shown Fig. 5, and zircon U–Pb analyses data and age results are listed in Table 2. In most cases, zircons from this sample occur as inclusions within other minerals, and usually preserve minor biotite, quartz and monazite inclusions. They are generally stubby and irregular in shape with length to width ratios of 1:1 to 2:1. They generally have core–rim structures, with dark, oscillatory or sector–zoned cores mantled by thin dark rims. Twenty–five spots were analyzed on twenty–four zircons from sample FY15–04, with U concentrations of 145–1444 ppm and relatively high Th/U ratios (0.16–0.52), which are consistent with zircons from HT–UHT metamorphic rocks (Yakymchuk et al., 2018 and

references therein). Similar zircons with relatively high Th/U ratios are also found from UHT granulite samples in this region (Tong et al., 2014). Zircons from this sample yield ^{206}U/^{238}U ages ranging from 251.4 to 503.7 Ma. Most zircon ages are distributed between 251.4 and 265.3 Ma, with a weighted mean age of 255.8 ± 1.8 Ma (n = 21, MSWD = 0.71) (Fig. 6). Two zircon cores give ^{206}Pb/^{238}U ages of 345.2 and 503.7 Ma, which are interpreted as inherited ones. And another two ^{206}Pb/^{238}U ages of 283.6 and 294.4 Ma might reflect mixture ages. The CL images are consistent with grains forming through re-crystallization during granulite facies metamorphism. Therefore, the U–Pb age of 255.8 ± 1.8 Ma is interpreted to reflect the timing of the low–pressure granulite facies metamorphic event in the southern Chinese Altay.

7. Discussion

7.1. Phase equilibrium modelling

A 10–compositional model system NCKFMASHTO (Na$_2$O–CaO–K$_2$O–FeO–MgO–Al$_2$O$_3$–SiO$_2$–H$_2$O–TiO$_2$–Fe$_2$O$_3$) was chosen to calculate the P–T pseudosections for the metapelitic gneiss samples FY15–04, FY15–14 and felsic gneiss sample FY15–32. Pseudosection calculations for sample FY15–32 (Fig. 7c) were carried out using THERMOCALC 3.40 (Powell and Holland, 1988), the internally consistent thermodynamic data set of Holland and Powell (2011) update ds62. The calculations for the other two samples (FY15–04 and FY15–14) (Fig. 7a and b) were performed using THERMOCALC 3.33 (Powell and Holland, 1988), with the internal thermodynamic data set ds55 s.txt (Holland and Powell, 1998; updated November 2003). Sillimanite and quartz are considered as pure phases. The a–x models used in the modelling and mineral abbreviations are shown in Supplementary File S6. The pseudosections for the investigated samples are presented in Figs. 7 and 8.

X–Ray fluorescence (XRF) data were converted to molar percent of the oxide and used as effective bulk rock compositions. Loss–on–ignition (LOI) of the whole–rock sample could provide a maximum estimate of H$_2$O. Considering the existence of other volatiles such as CO$_2$, half of these values were supposed to represent H$_2$O contents. The H$_2$O values are estimated at 2.13, 2.01 and 0.1 mol.%, respectively. The ferric iron contents of samples FY15–04, –14 and –32 are estimated at ∼7% mol.% of total iron based on the T–X(H$_2$O) pseudosection (not shown), and the corresponding X(O) values are 0.25, 0.37 and 0.18, respectively. MnO contents in all samples are negligible (< 0.31 wt.%). The pseudosections were constructed for the P–T range of 2.5–8.5 kbar and 650–900 °C (Fig. 7).

The constructed P–T pseudosection for the sample LT15–04 is shown in Fig. 7a. Garnet–absent phase assemblages are present in the relatively low–pressure region. The interpreted peak assemblage of opx + cd + pl + ksp + ilm + q + melt is predicted to be stable in the P–T range of < 5.0 kbar and > 800 °C. At higher pressure, the assemblages become garnet–present, whereas biotite is stable at lower temperature.

The P–T pseudosection calculated for the metapelitic gneiss LT15–14 is shown in Fig. 7b. One discrepancy between the predicted and observed assemblage is that minor K–feldspar is predicted in the modelling, but not observed in the sample FY15–14. This minor mismatch is likely due to an inappropriate bulk composition or to minor imperfections in the a–x models. Nevertheless, it has only minor effect on the underlying topology of the phase relations. The peak metamorphic assemblage (opx + cd + bi + pl + mt + ilm + q + melt) occupies a narrow field in the diagram. Up temperature, biotite leaves the assemblage, whereas at higher pressure magnetite is absent, and immediately down temperature the solidus is crossed. The actually measured x(opx) values approximately intersect the peak assemblage in a P–T range of < 5.0 kbar and 800–840 °C.

The P–T pseudosection calculated for the felsic gneiss LT15–32 is shown in Fig. 7c. Peak P–T conditions are constrained mainly by the
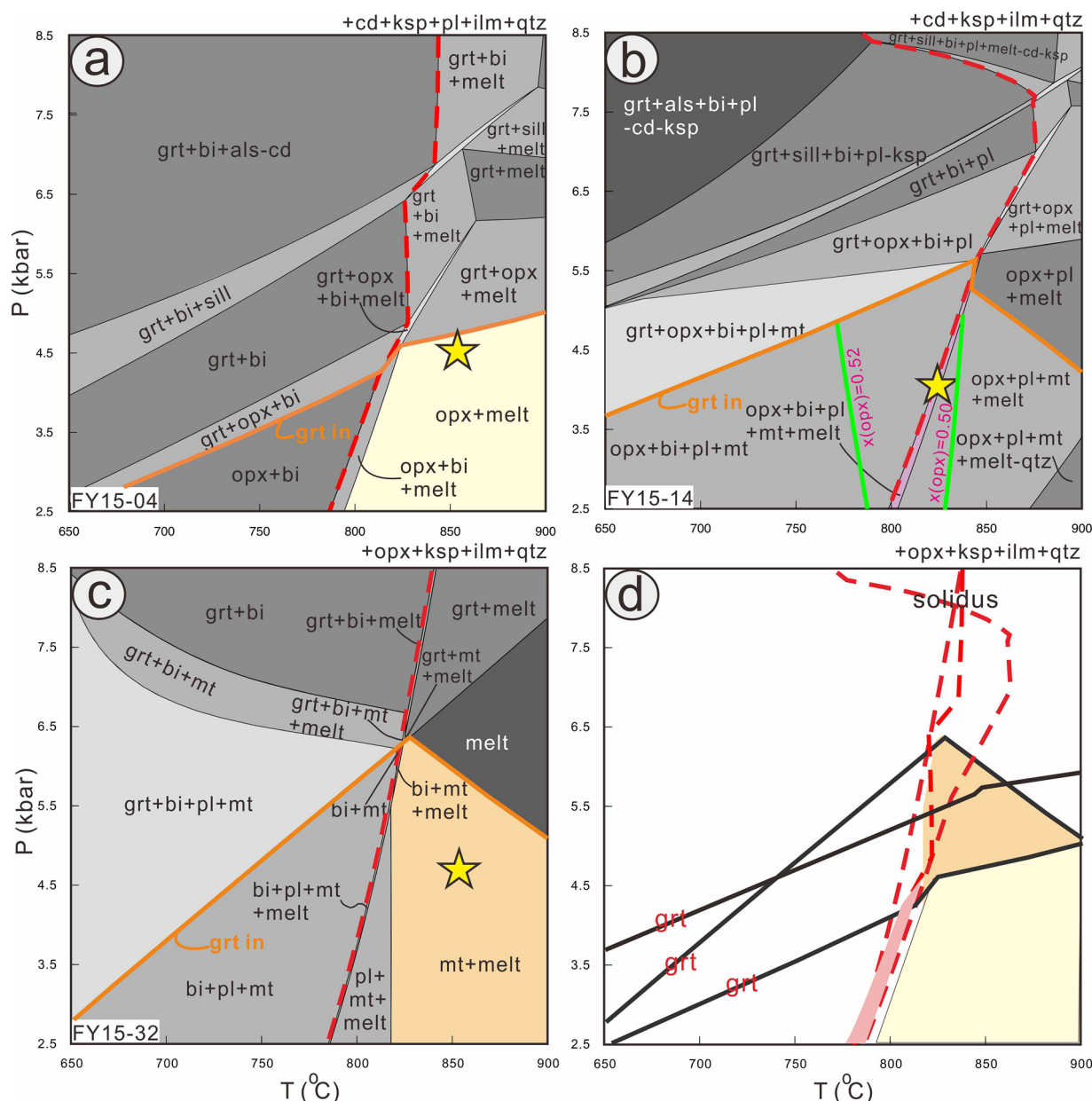
Fig. 7. The P–T pseudosections calculated for the Altay metapelitic and felsic gneisses. The red bold dashed lines represent the solidus. ★: peak P–T conditions. **a** P–T pseudosection for FY15–04. The bulk–rock composition was normalized as $SiO_2 = 65.14$, $Al_2O_3 = 12.82$, $CaO = 1.26$, $MgO = 6.06$, $FeO = 6.70$, $K_2O = 3.35$, $Na_2O = 1.54$, $TiO_2 = 0.73$, with $H_2O = 2.13$ and $O = 0.25$ mol.%. **b** P–T pseudosection for FY15–14. The particular bulk composition was estimated as $SiO_2 = 58.13$, $Al_2O_3 = 12.96$, $CaO = 1.39$, $MgO = 11.83$, $FeO = 9.91$, $K_2O = 1.34$, $Na_2O = 1.20$, $TiO_2 = 0.87$, $H_2O = 2.01$, $O = 0.37$ mol.%. **c** P–T pseudosection for the Altay felsic gneiss sample FY15–32. The particular bulk composition was estimated as $SiO_2 = 76.9$, $Al_2O_3 = 7.76$, $CaO = 0.32$, $MgO = 2.41$, $FeO = 4.74$, $K_2O = 5.45$, $Na_2O = 1.75$, $TiO_2 = 0.39$, $H_2O = 0.1$, $O = 0.18$ mol.%. **d** The predicted positions of solidus, garnet–absent lines, and stable fields of peak assemblages.

absence of peak plagioclase and the presence of magnetite. These combined constraints provide a P–T window of the peak metamorphic conditions of < 5.5 kbar and > 820 °C. The pseudosection calculated for FY15–32 with thermodynamic data set ds55 s is shown in Fig. 8. Some typical perthite grains are selected for analysis to retrieve the peak metamorphic temperatures. The reintegrated early single–phase feldspars are expected to contain albite contents of < 23.7 mol.%, which responds to a P–T range of 3.5–5.5 kbar and 850–900 °C.

The obtained P–T pseudosections are characterized by elevated solidus curves (at about 780–850 °C; Fig. 7d), suggesting that a certain amount of melt was lost from these rocks (i.e., they are residual rocks). Despite this process, phase equilibria modelling of residual compositions are thought to provide very robust constraints on the peak P–T conditions because the residual character may hamper solely the

reconstruction of the pre–peak evolution (see White et al., 2004; Bartoli, 2017, 2019; and references therein).

7.2. Peak P–T conditions and timing constraints

Peak metamorphic conditions and P–T paths of HT–UHT granulites and gneisses are shown in Fig. 9. Phase equilibria modelling for the Wuqiagou garnet–absent gneisses suggests that they have experienced low–pressure granulite–facies metamorphism with peak P–T conditions of 3.5–5.5 kbar/800–900 °C, which are slightly higher than that of hosted mafic granulite lenses (Li et al., 2004). This discrepancy is mainly due to the lack of appropriate thermometers suitable for the two–pyroxene mafic granulites.

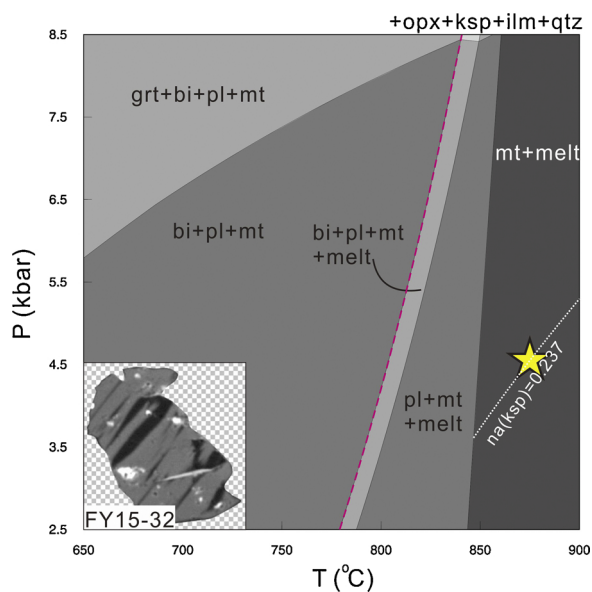UHT metapelitic granulites in this region have metamorphic ages of

Fig. 8. The P–T pseudosection calculated for FY15–32 using THERMOCALC 3.33, with the internal thermodynamic data set ds55 s. The pink bold dashed line is the solidus. The inset picture represents perthites with thin albite lamellae.
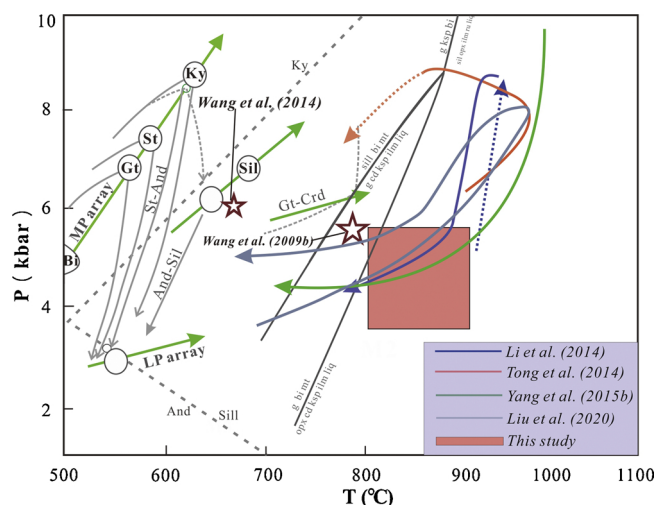

Fig. 9. Summary of P–T paths and metamorphic conditions of the HT–UHT granulites from the southern Chinese Altay (after Wei et al., 2007; Wang et al., 2009b, 2014; Li et al., 2014; Tong et al., 2014; Yang et al., 2015b; Liu et al., 2020).

290–280 Ma (Li et al., 2014; Tong et al., 2014; Liu et al., 2020). Metapelitic schists and granulites in Aletai city were dated at 299.2 ± 3.4 and 292 ± 2.3, respectively (Wang et al., 2009b, 2014). Regarding the timing of this phase of metamorphism, SIMS zircon U–Pb age analyses obtained from the Altay metapelitic gneiss sample FY15–04 yielded a weighted mean $^{206}Pb/^{238}U$ age of 255.8 ± 1.8 Ma, which is relatively later than previously published metamorphic ages. The low–pressure granulite–facies metamorphism at Wuqiagou area is probably associated with the late magmatic activities in the southern Chinese Altay. Besides, the mafic granulite lenses hosted within the opx–ksp gneiss also show a metamorphic age of ~255 Ma (Chen et al., 2006). This age is also highly coeval with the timing of the nearby mantle–derived mafic intrusions (~257 Ma) (Chen and Han, 2006), indicative of a regionally magmatic–metamorphic event in the late Permian in the southern Chinese Altay.

7.3. Tectonic implications

The tectonic process accounting for Permian thermal event has been and is still a controversial topic. In the southern Chinese Altay, all the precisely dated ophiolites in the eastern Junggar and the southern Altay are older than ca. 330 Ma (e.g., Wang et al., 2005; Zhang et al., 2010, 2012). Thus, it is reasonable to deduce that the amalgamation of Junggar terrain and the Chinese Altay occurred before Permian, possibly in the Carboniferous. Additionally, the Permian event is characterized by abundant late Paleozoic granitoids and gabbroic bodies with emplacement U–Pb zircon ages of 300–270 Ma (summarized in Table 1). These rocks are spatially concentrated along the southern flank of the Chinese Altay. Most Permian granitoids as well as coeval acidic dyke swarms have A– or I/A–type chemical signatures (Wang et al., 2005; Shen et al., 2013). These granitoids and voluminous contemporary mafic intrusions define a bimodal magmatic association (e.g., Wang et al., 2005; Shen et al., 2013), consistent with a post––orogenic extensional tectonic setting (Shen et al., 2013; Wang et al., 2009b, 2014; Liu and Tong, 2015; Liu et al., 2020). The P–T path of the Wuqiagou UHT granulites also indicates a post–orogenic extension in the Permian (Liu et al., 2020). Specifically, the occurrence of a decompression segment is consistent with the extensional thinning of a thickened crust. The crustal thickening characterized by a subsequent near–IBC is normally accompanied by underplating/accretion of deep–derived magma (Fig. 9; Liu et al., 2020).

Furthermore, the geochemistry of these plutons associated with the metapelitic and felsic gneisses in space and time indicates contributions from the deep mantle (Chen and Han, 2006). The Permian granites in Qinghe county were also considered to be generated from the mixing of pelitic and mantle materials (He et al., 2018). Combined with the regional geological background, the Permian magmatic–metamorphic events most likely occurred within an extensional setting (e.g., Wang et al., 2009b, 2014; Tong et al., 2014; Liu et al., 2020).

A regional significant event that is broadly coeval with the LP–HT metamorphism was the formation of the Permian–aged Large Igneous Province (LIP) in northwestern China (Zhang et al., 2012; Liu et al., 2014; Xu et al., 2014). Some recent studies have suggested that the Permian magmatism and extension were probably related to the rapid ascent of ponded plume magma beneath the lithosphere along the large Erqis fault belt (e.g., Chen and Han, 2006; Zhang et al., 2010, 2012; Shen et al., 2013; Yang et al., 2015a). Loury et al. (2018) has related the Permian magmatism and high–temperature metamorphism in the Pobeda area (Tien Shan range) to the Tarim mantle plume activities (e.g.,), indicating lateral flow focusing of the Tarim mantle plume has probably influenced the southwestern part of the CAOB. The Chinese Altay orogen is over 700 km to the Tarim basin (Windley and Xiao, 2018), and this phase of metamorphic event lagged > 20 Ma behind the plume–related activities. Therefore, Tarim mantle plume might contribute to the HT–UHT metamorphism in the early–middle Permian (Wang et al., 2014; Tong et al., 2014; Liu and Tong, 2015; Yang et al., 2015a; Liu et al., 2020). However, more evidence needs to be provided to support that the plume–related activities around the Tarim basin have lasted until the late Permian.

Collectively, the coeval bimodal magmatic activities in this region (e.g., Wang et al., 2005; Shen et al., 2013), the P–T paths documented by UHT granulites (Li et al., 2014; Tong et al., 2014; Liu et al., 2020), and cotemporaneous mantle–derived mafic intrusions (Chen and Han, 2006) are all indicative of a post–collisional extension setting with contributions from the deep mantle. Coupled with other geological observations, our preferred interpretation is that the high heat flux necessary for this metamorphism has been provided by underplating and heating of mantle–derived magmas at a relatively shallow crustal level (12–18 km), which have a possible genetic link with the Tarim mantle plume activities.

8. Conclusions

From a detailed metamorphic study of the garnet–absent metapelitic and felsic gneisses from Wuqiagou area, the conclusions concerning the evolution of the southern Chinese Altay orogenic belt in the late Paleozoic are:

(1) Garnet–absent metapelitic and felsic gneisses in the southern Chinese Altay were recognized for the first time in this study. They experienced partial melting and preserve supersolidus mineral assemblages. Phase equilibria modelling shows that these metapelitic and felsic gneisses have reached peak metamorphic P–T conditions of 3.5–5.5 kbar and 800–900 °C, recording a prominent low––pressure granulite–facies metamorphism in the southern Chinese Altay.
(2) The SIMS zircon U–Pb dating results suggest that the granulite––facies metamorphism occurred in the late Permian (255.8 ± 1.8). This age is highly coeval with the metamorphic timing of their hosted mafic granulite lenses (~255 Ma), which is also close to the emplacement age of nearby mantle–derived mafic plutons (~257 Ma).
(3) We propose that this low–pressure granulite–facies metamorphism might be associated with deep–derived mafic intrusions in a post–collisional extensional setting, with a possible link with the Tarim mantle plume activity.

Credit Author Statement

We here confirm that all the authors listed have contributions to this manuscript submitted to the journal of Geochemistry. The accurate and detailed descriptions of the authors' contributions to the work are:

Zhao Liu: He wrote the first draft of this paper and conducted most of the analysis in this paper.

Laixi Tong: He is the supervisor of Zhao Liu in China. He was involved in the field work, and provided the financial support to this study. Most importantly, he read this paper many times and proposed a lot of suggestions.

Omar Bartoli is the supervisor of Zhao Liu during his stay in University of Padova (Italy). He revised this paper and proposed a lot of suggestions and comments.

Bruna B. Carvalho also revised this paper and proposed a lot of suggestions and comments.

Chao Li finished the zircon U-Pb dating analysis with SIMS, and processed the chronological data

Declaration of Competing Interest

We here confirm that there are no conflicts of interest statements in the paper submitted to the journal of Geochemistry.

Acknowledgements

Appendix A. Supplementary data

Supplementary material related to this article can be found, in the online version, at https://doi.org/10.1016/j.chemer.2020.125603.

References

Bartoli, O., 2017. Phase equilibria modelling of residual migmatites and granulites: an evaluation of the melt–reintegration approach. J. Metamorph. Geol. 35, 919–942.

Bartoli, O., 2019. Reintegrating nanogranitoid inclusion composition to reconstruct the prograde history of melt–depleted rocks. Geosci. Front. 10, 517–525.

Bartoli, O., Acosta–Vigil, A., Tajčmanová, L., Cesare, B., Bodnar, R.J., 2016. Using nanogranitoids and phase equilibria modeling to unravel anatexis in the crustal footwall of the Ronda peridotites (Betic Cordillera, S Spain). Lithos 256–257, 282–299.

Barton, M.D., Hanson, R.B., 1989. Magmatism and the development of low–pressure metamorphic belts: implications from the western United States and thermal modelling. Geol. Soc. Am. Bull. 101, 1051–1065.

Bindu, R.S., 1997. Granulite facies spinel–cordierite assemblages from the Kerala Khondalite Belt, Southern India. Gondwana Res. 1, 121–128.

Briggs, S.M., Yin, A., Manning, C.E., Chen, Z.L., Wang, X.F., Grove, M., 2007. Late Paleozoic tectonic evolution history of the Ertix Fault in the Chinese Altay and its implications for the development of the Central Asian Orogenic System. Geol. Soc. Am. Bull. 119, 944–960.

Broussolle, A., Aguilar, C., Sun, M., Schulmann, K., Štípská, P., Jiang, Y.D., Yu, Y., Xiao, W.J., Wang, S., Míková, J., 2018. Polycyclic Palaeozoic evolution of accretionary orogenic wedge in the southern Chinese Altai: evidence from structural relationships and U–Pb geochronology. Lithos 314–315, 400–424.

Broussolle, A., Sun, M., Schulmann, K., Guy, A., Aguilar, C., Štípská, P., Jiang, Y.D., Yu, Y., Xiao, W., 2019. Are the Chinese Altai "terranes" the result of juxtaposition of different crustal levels during Late Devonian and Permian orogenesis? Gondwana Res. 66, 183–206.

Buick, I.S., Cartwright, I., Harley, S.L., 1998. The retrograde P–t–t path for low–pressure granulites from the Reynolds Range, central Australia: petrological constraints and implications for low–P/high–t metamorphism. J. Metamorph. Geol. 16, 511–529.

Chen, L.H., Han, B.F., 2006. Geochronology, geochemistry and Sr–Nd–Pb isotopic composition of mafic intrusive rocks in Wuqiagou area, north Xinjiang: constraints on mantle sources and deep processes. Acta Petrol. Sin. 22, 1201–1214 (in Chinese with English abstract).

Chen, H.L., Yang, S.F., Li, Z.L., Yu, X., Xiao, W.J., Yuan, C., Lin, X.B., Li, J.L., 2006. Zircon SHRIMP U–Pb chronology of the Fuyun basic granulite and its tectonic significance in the Altaid orogenic belt. Acta Petrol. Sin. 22, 1351–1358 (in Chinese with English abstract).

Craven, S.J., Daczko, N.R., Halpin, J.A., 2012. Thermal gradient and timing of high–T–low–P metamorphism in the Wongwibinda Metamorphic Complex, southern New England Orogen, Australia. J. Metamorph. Geol. 30, 3–20.

De Yoreo, J.J., Lux, D.R., Guidotti, C., 1991. Thermal modelling in low–pressure high––temperature metamorphic belts. Tectonophysics 188, 209–238.

Han, B., Ji, J., Song, B., Chen, L., Li, Z., 2004. SHRIMP zircon U–Pb ages of Kalatongke No.1 and Huangshandong Cu–Ni bearing mafic–ultramafic complexes, North Xinjiang, and geological implications. Chin. Sci. Bull. 49, 2424–2429.

He, D., Dong, Y., Xu, X., Chen, J., Liu, X., Li, W., Li, X., 2018. Geochemistry, geochronology and Hf isotope of granitoids in the Chinese Altai: implications for paleozoic tectonic evolution of the central Asian orogenic belt. Geosci. Front. 9, 1399–1415.

Holland, T.J.B., Powell, R., 1998. An internally consistent thermodynamic dataset for phases of petrological interest. J. Metamorph. Geol. 16, 309–343.

Holland, T.J.B., Powell, R., 2011. An improved and extended internally consistent thermodynamic dataset for phases of petrological interest, involving a new equation of state for solids. J. Metamorph. Geol. 29, 333–383.

Holness, M.B., Cesare, B., Sawyer, E.W., 2011. Melted rocks under the microscope: microstructures and their interpretation. Elements 7, 247–252.

Hu, A.Q., Wei, G.J., Deng, W.F., Chen, L.L., 2006. SHRIMP zircon U–Pb dating and its significance for gneisses from the southwest area to Qinghe County in the Altai, China. Acta Petrol. Sin. 22, 1–10 (in Chinese with English abstract).

Jahn, B.M., Windley, B., Natal'in, B., Dobretsov, N., 2004. Phanerozoic continental growth in central Asian. J. Asian Earth Sci. 23, 599–603.

Janoušek, V., Gerdes, A., Vrána, S., Finger, F., Erban, V., Friedl, G., Braithwaite Colin, J.R., 2006. Low–pressure granulites of the Lišov Massif, Southern Bohemia: viséan metamorphism of late devonian plutonic arc rocks. J. Petrol. 47, 705–744.

Jiang, Y.D., Sun, M., Zhao, G.C., Yuan, C., Xiao, W.J., Xia, X.P., Long, X.P., Wu, F.Y., 2010. The ~390 Ma high–T metamorphic event in the Chinese Altai: a consequence of ridge–subduction? Am. J. Sci. 310, 1421–1452.

Jiang, Y.D., Štípská, P., Sun, M., Schulmann, K., Zhang, J., Wu, Q.H., Long, X.P., Yuan, C., Racek, M., Zhao, G.C., Xiao, W.J., 2015. Juxtaposition of Barrovian and migmatite domains in the Chinese Altai: a result of crustal thickening followed by doming of partially molten lower crust. J. Metamorph. Geol. 33, 45–70.

Jiang, Y.D., Schulmann, K., Sun, M., Weinberg, R.F., Štípská, P., Li, P.F., Zhang, J., Chopin, F., Wang, S., Xia, X.P., Xiao, W.J., 2019. Structural and geochronological constraints on Devonian supra–subduction tectonic switching and Permian collisional dynamics in the Chinese Altai, central Asia. Tectonics 38, 253–280.

Langone, A., Godard, G., Prosser, G., Caggianelli, A., Rottura, A., Tiepolo, M., 2010. P–t–t path of the Hercynian low–pressure rocks from the Mandatoriccio complex (Sila Massif, Calabria, Italy): new insights for crustal evolution. J. Metamorph. Geol. 28, 137–162.

Laurent–Charvet, S., Charvet, J., Monié, P., Shu, L., 2003. Late Paleozoic strike–slip shear

zones in eastern central Asia (NW China): new structural and geochronological data. Tectonics 22, 237–241.

Li, Z.L., Chen, H.L., Yang, S.F., Xiao, W.J., Tainosho, Y., 2004. Discovery of the basic granulite from the Altai area: evidence from mineralogy. Acta Petrol. Sin. 20, 1445–1455 (in Chinese with English abstract).

Li, X.H., Liu, Y., Li, Q.L., Guo, C.H., Chamberlain, K.R., 2009. Precise determination of Phanerozoic zircon Pb/Pb age by multicollector SIMS without external standardization. Geochem. Geophys. Geosyst. 10, Q04010. https://doi.org/10.1029/2009GC002400.

Li, X.H., Tang, G.Q., Gong, B., Yang, Y.H., Hou, K.J., Hu, Z.C., Li, Q.L., Liu, Y., Li, W.X., 2013. Qinghu zircon: a working reference for microbeam analysis of U–Pb age and Hf and O isotopes. Chin. Sci. Bull. 58, 4647–4654.

Li, Z.L., Yang, X.Q., Li, Y.Q., Santosh, M., Chen, H.L., Xiao, W.J., 2014. Late Paleozoic tectono–metamorphic evolution of the Altai segment of the Central Asian Orogenic Belt: constraints from metamorphic P–t pseudosection and zircon U–Pb dating of ultra–high–temperature granulite. Lithos 204, 83–96.

Li, Q., Zhang, L.F., 2004. The P–T path and geological significance of low–pressure granulite–facies metamorphism in Muzhaerte, southwest Tianshan. Acta Petrol. Sin. 20, 583–594 (in Chinese with English abstract).

Liu, Z., Tong, L.X., 2015. The relationship between high–temperature metamorphism in Altay orogen and Tarim mantle plume: some evidence from mafic and metapelitic granulites. Acta Petrol. Sin. 31, 1761–1773 (in Chinese with English abstract).

Liu, H.Q., Xu, Y.G., Tian, W., Zhong, Y.T., Mundil, R., Li, X.H., Yang, Y.H., Luo, Z.Y., Shang–Guan, S.M., 2014. Origin of two types of rhyolites in the Tarim Large Igneous Province: consequences of incubation and melting of a mantle plume. Lithos 204, 59–72.

Liu, Z., Tong, L., Bartoli, O., Xu, Y.G., Huang, X., Li, C., 2019. Low–pressure metamorphism of mafic granulites in the Chinese Altay orogen, NW China: P–t path, U–Pb ages and tectonic implications. Solid Earth Sci. https://doi.org/10.1016/j.sesci.2019.11.004. (in press).

Liu, Z., Bartoli, O., Tong, L., Xu, Y.G., Huang, X., 2020. Permian ultrahigh–temperature reworking in the southern Chinese Altai: evidence from petrology, P–T estimates, zircon and monazite U–Th–Pb geochronology. Gondwana Res. 82, 20–40.

Long, X.P., Sun, M., Yuan, C., Xiao, W.J., Lin, S.F., Wu, F.Y., Xia, X.P., Cai, K.D., 2007. Detrital zircon age and Hf isotopic studies for metasedimentary rocks from the Chinese Altai: implications for the early Paleozoic tectonic evolution of the Central Asian Orogenic Belt. Tectonics 26, 1–19.

Long, X.P., Yuan, C., Sun, M., Kröner, A., Zhao, G.C., Wilde, S., Hu, A.Q., 2011. Reworking of the northern Tarim Craton by underplating of mantle plume–derived magmas: evidence from Neoproterozoic adakitic rocks in the Kuluketage area, NW China. Precambrian Res. 187, 1–14.

Loury, C., Rolland, Y., Lanari, P., Guillot, S., Bosch, D., Ganino, C., Jourdon, A., Petit, C., Gallet, S., Monié, P., Rief, N., 2018. Permian charnockites in the Pobeda area: implications for Tarim mantle plume activity and HT metamorphism in the South Tien Shan range. Lithos 304–307, 135–154.

Lucassen, F., Franz, G., 1996. Magmatic arc metamorphism: petrology and temperature history of metabasic rocks in the Coastal Cordillera of northern Chile. J. Metamorph. Geol. 14, 249–265.

Lux, D.R., De Yoreo, J.J., Guldotti, C., Decker, E.R., 1986. Role of plutonism in low––pressure metamorphic belt formation. Nature 323, 794–797.

Morrissey, L.J., Hand, M., Raimondo, T., Kelsey, D.E., 2014. Long–lived high–T, low–P granulite facies metamorphism in the Arunta Region, central Australia. J. Metamorph. Geol. 32, 25–47.

Okay, A.I., Sunal, G., Tüysüz, O., Sherlock, S., Keskin, M., Kylander–Clark, A.R.C., 2014. Low–pressure–high–temperature metamorphism during extension in a Jurassic magmatic arc, Central Pontides, Turkey. J. Metamorph. Geol. 32, 49–69.

Powell, R., Holland, T.J.B., 1988. An internally consistent dataset with uncertainties and correlations: 3. Applications to geobarometry, worked examples and a computer program. J. Metamorph. Geol. 6, 173–204.

Sandiford, M., Hand, M., McLaren, S., 1998. High geothermal gradient metamorphism during thermal subsidence. Earth Planet. Sci. Lett. 163, 149–165.

Sawyer, E.W., 2008. Atlas of migmatites. Mineralogical Association of Canada. The Canadian Mineralogist Special Publication 9, Quebec City. .

Schreurs, J., Westra, L., 1986. The thermotectonic evolution of a Proterozoic, low pressure, granulite dome, West Uusimaa, SW Finland. Contrib. Mineral. Petrol. 93, 236–250.

Shen, X., Zhang, H., Ma, L., 2013. LA–ICP–MS zircon U–Pb dating for jieerkuduke acidic Dykes in the Southern Altay Range. Xinjiang Geol. 31, 157–161 (in Chinese with English abstract).

Sláma, J., Košler, J., Condon, D.J., Crowley, J.L., Gerdes, A., Hanchar, J.M., Horstwood, M.S.A., Morris, G.A., Nasdala, L., Norberg, N., Schaltegger, U., Schoene, B., Tubrett, M.N., Whitehouse, M.J., 2008. Plešovice zircon–a new natural reference material for U–Pb and Hf isotopic microanalysis. Chem. Geol. 249, 1–35.

Sreejith, C., Kumar, G.R.R., 2012. MnNCKFMASH phase relations in Cordierite–orthopyroxene migmatitic gneisses, Southern India: implications for low–pressure crustal melting under Granulite–facies. J. Geol. Soc. India 80, 613–627.

Sun, M., Long, X.P., Cai, K.D., Jiang, Y.D., Wang, B.Y., Yuan, C., Zhao, G.C., Xiao, W.J., Wu, F.Y., 2009. Early Palaeozoic ridge subduction in the Chinese Altai: insight from the abrupt change in zircon Hf isotopic compositions. Sci. China (Series D) 39, 935–948 (in Chinese with English abstract).

The Team One of Geological Survey of Xinjiang, 1979. Four Geological Maps of Altai, With Geological Report, scale 1/200 000.

Thompson, A.B., England, P.C., 1984. Pressure–temperature–time paths of regional metamorphism II. Their inference and interpretation using mineral assemblages in metamorphic rocks. J. Petrol. 25, 929–955.

Tong, L., Xu, Y.G., Cawood, P.A., Zhou, X., Chen, Y.B., Liu, Z., 2014. Anticlockwise P–T evolution at ∼280 Ma recorded from ultrahigh–temperature metapelitic granulite in the Chinese Altai orogen, possible link with the Tarim mantle plume? J. Asian Earth Sci. 94, 1–11.

Tropper, P., Deibl, I., Finger, F., Kaindl, R., 2006. P–T–t evolution of spinel–cordierite–garnet gneisses from the Sauwald Zone (Southern Bohemian Massif, Upper Austria): is there evidence for two independent late–Variscan low–P/high–T events in the Moldanubian Unit? Int. J. Earth Sci. 95, 1019–1037.

Wang, T., Hong, D., Tong, Y., Han, B., Shi, Y., 2005. Zircon U–Pb SHRIMP age and origin of post–orogenic Lamazhao granite pluton from Altai orogen: its implications for vertical continental growth. Acta Petrol. Sin. 21, 640–650 (in Chinese with English abstract).

Wang, T., Hong, D.W., Jahn, B.M., Tong, Y., Wang, Y.B., Han, B.F., Wang, X.X., 2006. Timing, petrogenesis, and setting of Paleozoic synorogenic intrusions from the Altai Mountains, Northwest China: implications for the tectonic evolution of an accretionary orogeny. J. Geol. 114, 735–751.

Wang, T., Jahn, B.M., Kovach, P., Tong, Y., Hong, D.W., Han, B.F., 2009a. Nd–Sr isotopic mapping of the Chinese Altai and implications for continental growth in the central Asian orogenic Belt. Lithos 110, 359–372.

Wang, W., Wei, C.J., Wang, T., Lou, Y.X., Chu, H., 2009b. Confirmation of pelitic granulite in the Altai orogen and its geological significance. Chin. Sci. Bull. 54, 2543–2548 (in Chinese with English abstract).

Wang, W., Wei, C.J., Zhang, Y.H., Chu, H., Zhao, Y., Liu, X.C., 2014. Age and origin of sillimanite schist from the Chinese Altai metamorphic belt: implications for late Palaeozoic tectonic evolution of the Central Asian Orogenic Belt. Int. Geol. Rev. 56, 224–236.

Wei, C.J., Clarke, G., Tian, W., Qiu, L., 2007. Transition of metamorphic series from the kyanite– to andalusite–types in the Altai orogen, Xinjiang, China: evidence from petrography and calculated KMnFMASH and KFMASH phase relations. Lithos 96, 353–374.

White, R.W., Powell, R., Halpin, J.A., 2004. Spatially–focussed melt formation in aluminous metapelites from Broken Hill, Australia. J. Metamorph. Geol. 22, 825–845.

Wickham, S.M., Oxburgh, E.R., 1985. Continental rifts as a setting for regional metamorphism. Nature 318, 330–333.

Windley, B.F., Xiao, W.J., 2018. Ridge subduction and slab windows in the Central Asian Orogenic Belt: tectonic implications for the evolution of an accretionary orogeny. Gondwana Res. 61, 73–87.

Windley, B.F., Kröner, A., Guo, J.H., Qu, G.S., Li, Y.Y., Zhang, C., 2002. Neoproterozoic to Paleozoic geology of the Altai orogen, NW China: new zircon age data and tectonic evolution. J. Geol. 110, 719–737.

Windley, B.F., Alexeiev, D., Xiao, W., Kroner, A., Badarch, G., 2007. Tectonic models for accretion of the Central Asian Orogenic belt. J. Geol. Soc. 164, 31–47.

Xiao, W., Windley, B.F., Badarch, G., Sun, S., Li, J., Qin, K., Wang, Z., 2004. Palaeozoic accretion and convergent tectonics of the southern Altaids: implications for the growth of Central Asia. J. Geol. Soc. 161, 339–342.

Xu, Y.G., Wei, X., Luo, Z.Y., Liu, H.Q., Cao, J., 2014. The early permian tarim large igneous province: main characteristics and a plume incubation model. Lithos 204, 20–35.

Yakymchuk, C., Kirkland, C.L., Clark, C., 2018. Th/U ratios in metamorphic zircon. J. Metamorph. Geol. 36, 715–737.

Yang, T.N., Li, J.Y., Zhang, J., Hou, K.J., 2011. The Altai–mongolia terrane in the Central Asian Orogenic Belt (CAOB): a peri–gondwana one? Evidence from zircon U–Pb, Hf isotopes and REE abundance. Precambrian Res. 187, 79–98.

Yang, T.N., Li, J.Y., Liang, M.J., Wang, Y., 2015a. Early Permian mantle–crust interaction in the south–central Altaids: high–temperature metamorphism, crustal partial melting, and mantle–derived magmatism. Gondwana Res. 28, 371–390.

Yang, X.Q., Li, Z.L., Wang, H.H., Chen, H.L., Li, Y.Q., Xiao, W.J., 2015b. Petrology and geochemistry of ultrahigh–temperature granulites from the South Altay orogenic belt, northwestern China: implications for metamorphic evolution and protolith composition. Isl. Arc 24, 169–187.

Zhang, C.L., Li, Z.X., Li, X.H., Xu, Y.G., Zhou, G., Ye, H.M., 2010. A Permian large igneous province in Tarim and Central Asian orogenic belt, NW China: results of a ca. 275 Ma mantle plume? Geol. Soc. Am. Bull. 122, 2020–2040.

Zhang, C.L., Santosh, M., Zou, H.B., Xu, Y.G., Zhou, G., Dong, Y.G., Ding, R.F., Wang, H.Y., 2012. Revisiting the "Irtish tectonic belt": implications for the Palaeozoic tectonic evolution of the Altai orogeny. J. Asian Earth Sci. 52, 117–133.

Zhang, Y., Chen, J.L., Bai, J.K., Tang, Z., 2015. LA–ICP–MS zircon dating of gneissic granitic intrusive mass in Wuqiagou on the southern margin of Altay Orogenic Belt and its geological significance. Northwestern Geol. 48, 127–139 (in Chinese with English abstract).

Zhang, J.R., Wei, C.J., Chu, H., 2018. High–t and low–P metamorphism in the Xilingol Complex of central Inner Mongolia, china: an indicator of extension in a previous orogeny. J. Metamorph. Geol. 36, 393–417.

Zheng, C.Q., Xu, X.C., Kato, T., Enami, M., 2007. Permian CHIME ages of monazites for the kyanite–sillimanite type metamorphic belt in Chonghuer area, Altai, Xinjiang and their geological implications. Geol. J. China Univ. 13, 566–573 (in Chinese with English abstract).

Zhou, G., Zhang, Z.C., Luo, S.B., He, B., Wang, X., Ying, L.J., Zhao, H., Li, A.H., He, Y.K., 2007. Confirmation of high–temperature strongly peraluminous Mayin'ebo granites in the margin of Altay, Xinjiang: age, geochemistry and tectonic implications. Acta Petrol. Sin. 23, 1909–1920 (in Chinese with English abstract).

Zhuang, Y.X., 1994. The PTSt evolution of metamorphism and development mechanism of the thermal–structural–gneiss domes in the Chinese Altaides. Acta Geol. Sin. 68, 35–47 (in Chinese with English abstract).